Theoretical analysis of earth-abundant solar cell based on green absorber CuFeO$_2$

D. Prasad[1] · G. Anitha[2] · L. Megalan Leo[3] · Atul Kumar[4]

Abstract

Huge advancements in the understanding of photovoltaic (PV) physics have been made, but still, PV has not overtaken conventional energy sources due to PV materials cost, toxicity, and stability concerns. In the pursuit of discovering a new solar energy harvester which satisfies criteria such as low cost, earth-abundance, non-toxicity, high efficiency and long-term stability, extensive research has been conducted on the potential of copper iron oxide (CuFeO$_2$), also known as delafossite oxide. CuFeO$_2$ possesses optimal bandgap (1.5 eV), with a high absorption coefficient and carrier mobility, suitable for potentially cost-effective solar cells. Theoretical modelling based on the optical and electrical characteristics of the CuFeO$_2$ system is performed here on delafossite CuFeO$_2$ to examine its photovoltaic performance. We explored various buffer counterparts for CuFeO$_2$ absorber, and a stack of $p–n^+–n^{++}$ *is* simulated for device optimization. ZnO showed zero conduction band offset with CuFeO$_2$ and a corresponding efficiency of 28% for CuFeO$_2$/ZnO/ITO ($p–n^+–n^{++}$) device. The optimal range of crucial design parameters, such as doping profile, absorber thickness, surface recombination velocity, back contact work function, resistances, and bulk defects, that allow CuFeO$_2$ solar cells to reach power conversion efficiencies above 25% are quantified. The spectrum loss (thermalization and non-absorption loss) stands at 59.6%, extrinsic recombination loss at 12.3%, and the performance ceiling of CuFeO$_2$ at 28.1%. Theoretical analysis shows that the maximum achievable efficiency of 28% is close to the Shockley–Queisser (S–Q) limit and comparable to contemporary inorganic solar cells. The findings presented in this study are anticipated to stimulate experimentalists to fabricate stable, high-efficiency CuFeO$_2$-based thin film solar cells.

1 Introduction

The cuprous delafossite oxides, composed of $Cu^{1+}M^{3+}O_2$ (where M represents a trivalent transition-metal cation like Fe, Cr, Al, etc.), possess tuneable optoelectrical properties (Xu et al. 2021; Ferri et al. 2020). Consequently, their exceptional properties make them highly sought after for their ability to absorb light in thin-film solar cells. The delafossite oxides

---

(ABO$_2$) are named after the French scientist Gabriel Deloffose, where A is a transition, alkali, or alkaline metal, B is the transition metal, and O is the oxygen (Crespo 2018). Among the cuprous delafossites, CuFeO$_2$ has an ideal bandgap for absorbing the terrestrial AM1.5G spectrum (with E$_g$ approximately 1.5 eV) (Jiang et al. 2019a). It consists of elements abundant in the earth's crust, (Ferri et al. 2020) environmentally friendly, thermally, and chemically stable, (Deng et al. 2023; Prévot et al. 2015) and can be produced using various scalable and cost-effective deposition methods (Deng et al. 2023; Prévot et al. 2015; Jin and Chumanov 2016; Singh et al. 2019; Song et al. 2016; Gonzaga and Mercado 2022; Zhu et al. 2016). The fabrication of CuFeO$_2$ is reported by techniques such as sputtering, pulsed laser deposition, and cost-effective non-vacuum methods like sol–gel-based spin coating, hydrothermal method, spray pyrolysis and electrodeposition (Prévot et al. 2017; Li et al. 2023; Shaili et al. 2021; Son 2022a). Due to its properties, delafossite compounds have found various optoelectronic applications, including hole transport material (HTM) in perovskite, (Akin et al. 2019) in dye-sensitized solar cells, (Zhu et al. 2016) PEC water splitting, (Prévot et al. 2015) CO$_2$ splitting, (Gonzaga and Mercado 2022) transparent conducting oxide semiconductor (Xu et al. 2021) and solar energy harvester (Crespo 2018).

The efficiency of photovoltaic systems is a complex function of material properties, such as their ability to absorb light, bandgap, carrier's lifetime, tendency to undergo non-radiative recombination, etc. There is a significant quest to identify materials that can effectively convert sunlight into energy in a reliable, cost-effective, and efficient manner, and this is a significant hurdle in our journey toward sustainable green energy sources. In this regard, CuFeO$_2$ presents bright prospects as a sustainable, environmentally friendly, nontoxic, and economical absorber for solar cells. Vojkovic et al. (2019) reported pulsed laser deposition of CuFeO$_2$ films. The obtained films showed photoconductivity with light-dependent resistivity. Liu et al. synthesized single-phase, high-purity and highly crystalline CuFeO$_2$ using an optimized hydrothermal process (Liu et al. 2020a, 2020b). They showed a stable solar energy conversion using CuFeO$_2$ as a photocatalyst in an aqueous and reductive environment, demonstrating the exception stability of CuFeO$_2$ and absorption property. Karmakar et al. fabricated heterojunction by electrodeposition of *p*-type CuFeO$_2$ over *n*-type ZnO substrate, effectively making a *p–n* junction (Karmakar et al. 2017). The heterojunction showed high visible light absorption, effective charge carrier (electron–hole) separation and long stability. Akin et al. fabricated a *n–i–p* perovskite solar cell and utilized CuFeO$_2$ as *a p*-type layer in this device configuration (Akin et al. 2019). CuFeO$_2$ hole transport layer-based non-encapsulated perovskite solar cells exhibited superior self-stability and retained over 90% of their initial PCE even at 80% relative humidity. Son et al. (2022b) fabricated CuFeO$_2$ film by the galvanostatic electrodeposition followed by annealing in inert gas. Fugate et al. (2019) electrodeposited CuFeO$_2$ and summarised Cu vacancies O interstitials defects causing its *p*-type nature. Alkallas et al. (2022) demonstrated direct combustion of Cu foil coated with Fe$_2$O$_3$ nanomaterials, leading to the formation of CuFeO$_2$. This freestanding CuFeO$_2$/CuO foil showed optoelectronic application with high photoresponsivity and detectivity in the visible region. Jiang et al. (2019b) prepared CuFeO$_2$ by spin coating and showed heterojunction could effectively separate photogenerated electron–hole pair and their recombination. Shaili et al. (2021) deposited CuFeO$_2$ thin film via spray-coated, revealing *p*-type conductivity with tunable resistivity. Similar optoelectronic applications are widely reported, demonstrating CuFeO$_2$'s advantageous visible light absorption property.

The optoelectronic properties of CuFeO$_2$ arise from its crystal structure. The structure of CuFeO$_2$ consists of alternating layers of Cu and Fe (Xu et al. 2021). Every oxygen atom is coordinated by one Cu$^+$ cation and three M^{3+} cations. Delafossite oxides crystalize into

two rhombohedral structures with space group R3m and hexagonal structures with space group P63 (Jiang et al. 2019a). The slope of VB maxima and CB minima determine the effective masses of charge carriers (thus controlling the mobility) and the dynamics of photoexcited carriers (low exciton binding). It determines the nature of band gap and optoelectronic properties. The maxima of valence band states are contributed by the Cu 3d orbitals along with the hybridization from O 2p states, whereas nonbonding Fe 3d orbitals contribute to the conduction band minima states (Gonzaga and Mercado 2022). The excitation of an electron from O 2p states in the valence band to conduction band Fe 3d states characterizes the primary optical transition in $CuFeO_2$ (CFO). This transition is promptly followed by a thermalization process within the valence band, which involves the holes generated from O 2p states transfer to Cu 3d valence band states. This transfer can be visualized as an electron movement from Cu 3d states to fill the holes in the deeper O 2p states. The thermalization of holes is advantageous and plays a crucial role in facilitating the separation of charges within the lattice and effectively reducing electron–hole recombination. This effect is attributed to the absence of covalent bonding between the Cu and Fe atoms. Consequently, the hole thermalization process is believed to be accountable for the longer carrier lifetime, durability, and excellent photoactivity exhibited by $CuFeO_2$ compared to its parent binary oxide, Cu_2O (Jin and Chumanov 2016). $CuFeO_2$ exhibits p-type conductivity, resulting from native Cu vacancies and O interstitials in its structure (Gonzaga and Mercado 2022), and transition metal cation controls the bandgap in the copper delafossites. The well-known copper-based p-type oxide semiconductor, CuO (solar cell absorber), undergoes photo-corrosion and degradation, whereas the $CuFeO_2$ (CFO) exhibits enhanced stability (Ferri et al. 2020). In particular, CFO demonstrates greater chemical stability when exposed to illumination and aqueous environments compared to binary copper oxide compounds (Deng et al. 2023). The CMO_2 oxides are nontoxic, abundant (exclusively made of atoms abundant in the earth's crust), and stable up to 800 °C (Gottesman et al. 2021). CFO possesses several favourable characteristics, including higher absorption coefficients ($> 10^5$ cm^{-1}), an appropriate bandgap (~ 1.5 eV), long carrier lifetime (~ 200 ns), (Prévot et al. 2017) good carrier mobility (0.2 cm^2/Vs) and high conductivity (Li et al. 2023). These properties result in smaller absorption depths, which, in turn, promote efficient carrier extraction while minimizing carrier recombination (Jin and Chumanov 2016).

　　Surprisingly, despite its potential as a promising light absorber, no studies have investigated using $CuFeO_2$ as a material for solar cell absorbers. Consequently, we have pioneeringly utilized stable and cost-effective $CuFeO_2$ as a highly efficient inorganic absorber for solar cell application. CFO material holds the potential to offer long-term stability and cost-effective photovoltaic performance owing to its earth abundance. Section 2 describe the device configuration/architecture and simulation methodology utilized for designing CFO-based solar cell. Section 3 describe the theoretically achievable efficiency of CFO-based solar cell under various recombination regimes.

2 Device architecture and simulation approach

Empirically photovoltaic efficiency (η) is given as

$$\eta = \frac{V_{OC} \times J_{SC} \times FF}{P_{in}} \tag{1}$$

where V_{OC} is the open circuit voltage, FF is the fill factor, J_{SC} is the short circuit current, and P_{in} is the incident solar power, which is a function of terrestrial solar spectrum S(E). The V_{OC} depends on the absorber and is given by Kar et al. (2021)

$$V_{OC} = 1/q\left(E_G - V_{Loss}\right) \tag{2}$$

where V_{Loss} is the voltage loss due to recombination, E_G is the absorber bandgap. Under instantaneous illumination, a significant quantity of photogenerated electrons accumulates in the conduction band, while many holes gather in the valence band. As a result, separate Fermi levels for electrons and holes are formed. The extent of separation between electrons and holes at the Fermi level is the net conversion of solar heat into chemical potential, leading to the generation of V_{OC} in the device. The J_{SC} is primarily the function of the absorber bandgap. The J_{SC} is empirically given by

$$J_{SC} = q \int_{E_G}^{\infty} \frac{S(E)}{E} dE \tag{3}$$

The variables q, E, and S(E) represent the electronic charge, the energy of the incoming photons, and the spectral power per unit area of the incident light, respectively. Incident photons with energy lower than the bandgap are transmitted and considered non-absorption losses. Photons with energy greater than the bandgap energy are absorbed; among these photons, only energy equal to E_G will contribute to the current, while any excess energy will be lost as thermalization. The fill factor (FF) is influenced by the quality of the device interface and resistance values, and it ideally has a value of 1. FF follows the V_{OC} trend under various recombination regimes.

In this numerical study, we utilized a one-dimensional Poisson solver SCAPS (Burgelman et al. 2000) version 4.02 (solar cell capacitance simulator), which solves Poisson and continuity equations under illumination (generation) and recombination (bulk and interfacial recombination) (Gomathi et al. 2023a, 2023b; Kumar et al. 2022, 2021; Prabu et al. 2023; Livingston et al. 2023; Reddy et al. 2022).

The one-dimensional Poisson-Schrodinger solver solves a set of interconnected equations, including Poisson's equation, continuity equation, drift–diffusion equation, and generation-recombination profiles. It utilizes Gummel iteration coupled with Newton–Raphson substeps along the p–n^+ stack length to model the device working. The solver is applied at the bulk and interface of the device, considering various illumination and biasing conditions. By applying appropriate boundary conditions at the interfaces and contacts, the solver solves the interconnected differential equations as shown,

$$J_n = -\frac{\mu_n n}{q} \frac{dE_{Fn}}{dx} \tag{4}$$

$$J_p = \frac{\mu_p p}{q} \frac{dE_{Fp}}{dx} \tag{5}$$

$$-\frac{dJ_n}{dx} - U_n + G = \frac{dn}{dt} \tag{6}$$

$$-\frac{dJ_p}{dx} - U_p + G = \frac{dp}{dt} \tag{7}$$

$$\frac{d}{dx}\left(\varepsilon_0 \varepsilon_r \frac{d\Psi}{dx}\right) = -q\left(p - n + N_D^+ - N_A^- + \frac{\rho_{def}}{q}\right) \tag{8}$$

In the given Eqs. 4–7, variables n and p refer to the carrier density, Ψ represents the electrostatic potential, ρ_{def} is defect density, variables J_n and J_p correspond to the electron and hole current density, symbol $\mu_{p/e}$ represents the hole/electron mobility, E_{Fn} and E_{Fp} represent the electron and hole Fermi level, G signifies the generation rate, U is the recombination rate while ε_0 and ε_r denote the permittivity of vacuum and semiconductor, respectively. The N_D^+ and N_A^- represent the density of donors and acceptors. Equations 1 and 2 pertain to charge carrier transport, whereas Eqs. 3–4 relate to the continuity of electrons and holes; Eq. 5 represents the Poisson equation. To simulate tunnelling and conduction band offset at junctions and interfaces, SCAPS employs the WKB approximation, a semi-classical approach. The electrostatic potential, generation, and quasi-Fermi levels are calculated using the AM1.5G illumination. The simulation considers the ideal Shockley–Read–Hall (SRH) recombination lifetime due to considerable advancement in fabrication technologies, which enable devices to avoid non-radiative losses. In the simulation, a uniform optical absorption constant $\alpha(\lambda)$ is utilized, as per the bandgap of the absorber.

The device configuration under investigation is $p/n^+/n^{++}$. The CuFeO$_2$ is a p-type absorber, and various n^+ buffer layers such as ZnO, SnO$_2$, CdO, and MoO$_3$ are examined for their compatibility for heterojunction with CFO. The simulations are performed by taking the material parameters from the literature and are comprehensively summarized in Table 1. Our device and results can be reproduced by using the parameters from Table 1 (Deng et al. 2023; Zhu et al. 2016).

Table 1 Material parameters utilized in the simulation. (Zhu et al. 2016)

Symbol	Quantity	CuFeO$_2$ Values
t	Thickness (µm)	0.2
E_G	Bandgap (eV)	1.5
EA	Electron affinity (eV)	3.9
NC	Conduction band density of state, (cm^{-3})	2×10^{18}
NV	Valence band density of state, (cm^{-3})	10^{19}
α	Absorption coefficients (1/cm)	10^5
V$_{th}$	Electron thermal velocity (cm/s)	10^7
V$_{th}$	Hole thermal velocity (cm/s)	10^7
p	Hole density (cm^{-3})	10^{16}
μ_e	Electron mobility, (cm^2/Vs)	900
μ_h	Hole mobility (cm^2/Vs)	200

3 Results and discussion

3.1 CuFeO₂ device and buffer layer selection

The proposed configuration of the CuFeO₂/ZnO/ITO-based solar cell device is shown schematically in Fig. 1. The device p–n^+–n^{++} configuration of CuFeO₂/ZnO/ITO shows the device's initial parameters, i.e. the stack arrangement thickness of each layer, is schematically illustrated. The crystal structure of CuFeO₂, as shown in Fig. 1a, was plotted using cif file in Diamond software. Figure 1c shows the simulated emission spectrum of the CFO absorber layer using AFORS-HET software (Stangl et al. 2006). Most incident photons with wavelength ($\lambda \leq 825$) are absorbed within the CFO absorber (Forslund 2016). The reported CFO bandgap is 1.5 eV (Liu et al. 2020a). This bandgap value is near ideal for optimal solar spectrum absorption. The theoretical Shockley-Quizzer (SQ) efficiency limit for bandgap 1.5 eV is 32% (Hemalatha et al. 2023). CFO's simulated photoluminescence (PL) shows the PL emission peak at 900 nm. The emission peaks occur near the bandgap of CFO. The PL spectra for CFO highlights its potential prospects as an excellent visible spectrum absorber and applicability as an absorber in solar cell device.

We explored various compatible buffer counterparts for CFO absorbers to make an efficient p-n^+ heterojunction. The prospective buffer layer requires a wide bandgap with high electron density higher than the majority carrier concentration in CFO. Table 2 summarizes the oxides n-type materials. Most oxide materials reported here are n^+ type with electron density higher than 10^{18} cm^{-3}, except V₂O₅ and MoO₃. The bandgap of n-type oxides ranges from 2 to 6 eV. Fe₂O₃ and CdO have a bandgap in the lower range of ~ 2 eV, whereas Al₂O₃ have a bandgap of ~ 6 eV. Electron affinity of the buffer layer enables it to make a suitable energy level matching; this is one of the crucial parameters for controlling interfacial phenomena such as recombination and carrier collection and is an optimal design consideration. These strict material properties requirements provide guidelines to filter out unsuitable and prospective n-type oxides for the buffer layer. Figure 2 presents the energy level matching (the conduction band and valence band levels) with that of the CFO. Due to their optimal material parameters, we have explored ZnO, CdO and MoO₃ as buffer layers for CFO-based devices. The MoO₃ makes a spike-type
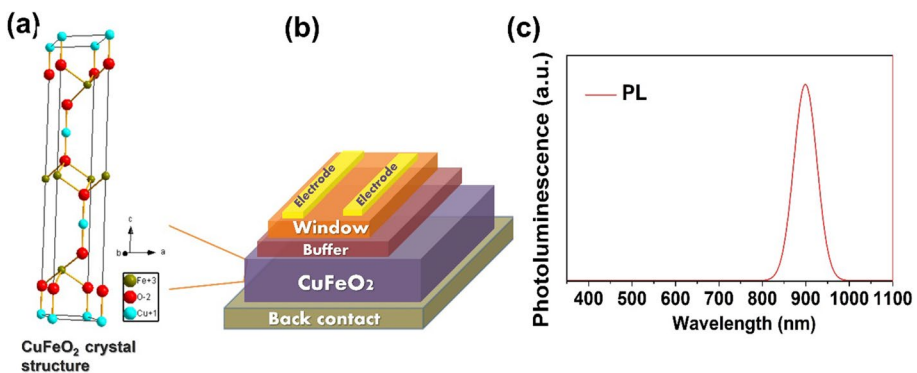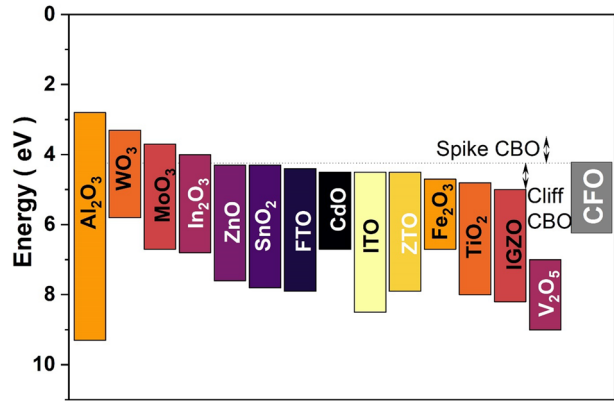

Fig. 1 **a** The crystal structure of CuFeO₂ absorber. **b** The schematic of the proposed CFO device. **c** The simulated photoluminescence spectra for the CuFeO₂/ZnO/ITO solar cell device

Fig. 2 The energy level (conduction band CB, valence band VB, and bandgap Eg) of the common *n*-type oxide material explored for the buffer layer counterpart for the CFO absorber

alignment, the CdO makes a cliff-type alignment, and the CFO/ZnO have a matching alignment at the interface (Table 2).

The simulated band diagram of CFO based device with different buffers is shown in Fig. 3. The simulated band diagram plot shows the device stack, the thickness of each layer, their respective band gaps, each layer's electron affinity, and the band bending regions in the device. The $CuFeO_2/MoO_3/ITO$, $CuFeO_2/CdO/ITO$ and $CuFeO_2/ZnO/ITO$ devices are plotted, showing their respective energy levels matching at the interface. The high carrier (electron) density in the *n*-type buffer window layer causes band bending in the *p*-type region. This is a desirable condition which is purposely incorporated by choosing a doping profile. The carrier collection at the heterojunction of CFO/buffer is optimal in p–n^+–n^{++} configuration. The EC (conduction band level) in CFO and buffers (MoO_3, CdO, ZnO) is different, and they make a different band alignment, as shown in Fig. 3a–c. The corresponding electron affinities cause this spike and cliff band alignment.

The simulated device efficiency of the CFO device with MoO_3, ZnO and CdO buffer is shown in Fig. 4a. The MoO_3 have lower efficiency than the CFO/CdO and CFO/ZnO device. The MoO_3 have a positive conduction band offset, the spike-type alignment. The conduction band offset (CBO) is given by electron affinity different from heterojunction counterparts and empirically given as $CBO = EA_{CFO} - EA_{Buffer}$. The efficiency is best for the CFO/ZnO heterojunction as they have zero conduction band offset. The high CBO barrier in positive (spike) and negative (cliff) damages device performance. The inset image shows the schematic of the band alignment of the spike and cliff type at the interface. The high cliff-type alignment will increase the probability of interfacial recombination, as shown in the inset of Fig. 4b. The high spike barrier hinders carrier transport, thus decreasing device performance. It is observed that zero CBO and a slight spike barrier are optimal for device performance.

The probability of occupation of interface states by electrons and holes controls overall interfacial recombination. The conduction band offset at absorber/buffer, with cliff and spike type alignment, is schematically shown in Fig. 5. The interface recombination pathway for the cliff is marked in Fig. 5a, and the spike is marked in Fig. 5b. Spike alignment has a wide interface as compared to cliff alignment. Wide interfaces in spike alignment have a lower probability of recombination than cliff alignment. The wide front bandgap of absorber alters the conduction band offset (CBO) in device. CBO is given by

Table 2 Summary of physical properties of n-type oxide materials. (Elumalai et al. 2015; Shi et al. 2021)

Material	Bandgap (eV)	Semiconductor type	Electron mobility (cm^2/Vs)	Electron density (cm^{-3})	Electron affinity (eV)	Conductivity (Scm^{-1})
ZnO	3.3–3.4	n	100–200	10^{18}–10^{19}	4.3 (Shi et al. 2021)	5000
SnO$_2$	3.5–3.7	n	200	10^{18}	4.3	2000
Fe$_2$O$_3$	1–9–2.2	n	–	10^{19}	4.7	Liu et al. (2013)
TiO$_2$	3.2	n	100	10^{18}	4.8–5	Singh et al. (2021)
WO$_3$	2.5–3	n	15	10^{19}	3.3	–
MoO$_3$	3	n	1000 (Scanlon et al. 2013)	10^{15}	3.7	Dandogbessi and Akin–Ojo (2016)
ITO	4	n	50	10^{20}	4.5–4.7	1000
FTO	3.5–4	n	50	10^{20}	4.4	10^4
Al$_2$O$_3$	6.5	n	50 (Egbo et al. 2021)	10^{17}	2.8	Ryu et al. (2020)
CdO	2.2	n	100	10^{20}	4.5	10^4
In$_2$O$_3$	2.8–2.9	n	100–300	10^{19}	4	10,000
ZTO	3.4	n	20	–	–	250 (Lee et al. 2019)
IGZO	3.2	n	80	10^{20}	5	200
V$_2$O$_5$	2	n	20	10^{15}	7	Medhi et al. (2019)

Fig. 3 **a** The energy band diagram of all CFO/MoO₃/ITO, **b** CFO/ZnO/ITO, **c** CFO/CdO/ITO
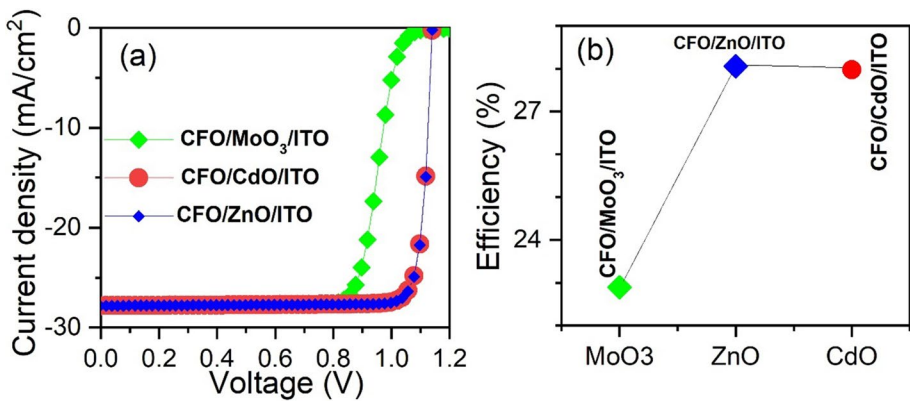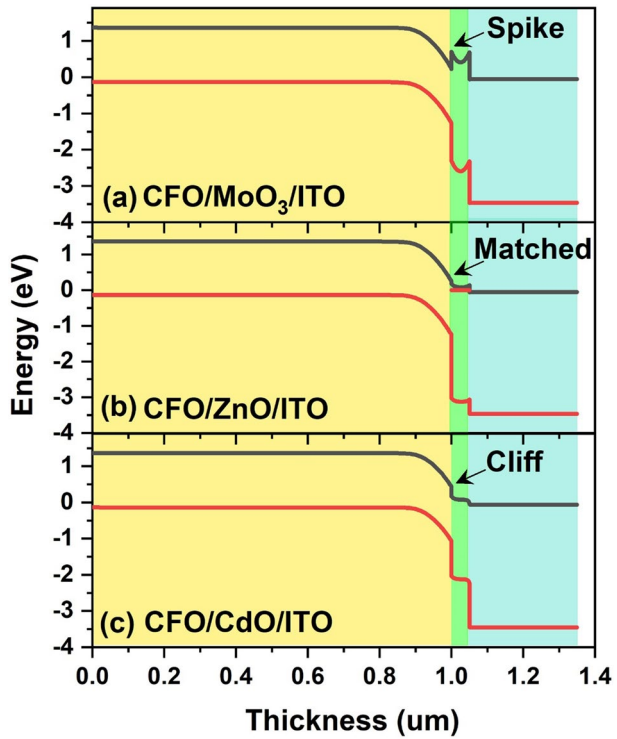

Fig. 4 **a** Comparative J–V plot of CFO/MoO₃/ITO, CFO/CdO/ITO, CFO/ZnO/ITO solar cells. The J–V plot of CFO/CdO/ITO and CFO/ZnO/ITO overlap. **b** The CFO/ZnO/ITO device is most efficient due to zero conduction band offset at the CFO/ZnO interface

$$E_{CBO} = \left(EA_{abs} - EA_{buffer} \right)$$

where EA is the electron affinity. CBO (E_{CBO}) is negative for cliff-type alignment and positive for spike-type alignment. Ideally, CBO should have zero or slightly positive spike alignment to lower interfacial recombination. Even though spike alignment creates
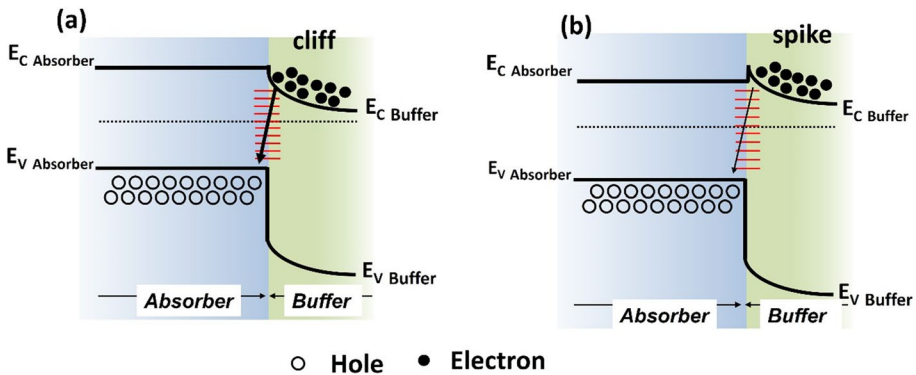
Fig. 5 **a** The cliff-type conduction band offset alignment shows elevated interfacial recombination through interface states at the absorber/buffer junction. **b** The spike-type conduction band offset alignment shows a wider interfacial gap and reduced interfacial recombination

a barrier for charge transport, small positive barriers up to 0.1 eV are benign. As seen in the schematic, the interface is wider for spike alignment, which decreases the recombination probability of electrons from the conduction band of the buffer and holes from the valence band of the absorber. Similar physical reasoning of small positive spike-type band alignment are reported in the literature for lowering interfacial recombination (Kumar and Ajay 2018; Minemoto and Murata 2015). On the other hand, cliff-type alignment lowers the interfacial gap, increasing the recombination probability of electrons from the conduction band of the buffer and holes from the valence band of the absorber.

3.2 Optimization of carrier density

The efficiency of CFO/ZnO/ITO is plotted for the carrier density of the absorber and the buffer layer. The background doping profile of the absorber and buffer controls the recombination profile and charge separation at the absorber/buffer interface. Higher hole density in the absorber layer makes a p^+n configuration, whereas the high electron density in the buffer will make the device a $p\text{-}n^+$ configuration. The $p\text{-}n^+$ configuration is advantageous as the depletion region is shifted in the absorber region, drifting the photogenerated carrier toward the buffer side and expediting carrier collection. The p^+n configuration will have a depletion region in the buffer region, a suboptimal condition for carrier separation. The simulation plot in Fig. 6 shows the efficiency dependence on the absorber and buffer respective carrier density. The efficiency is highest for CFO hole density of 10^{16} cm^{-3} and buffer electron density of 10^{18} cm^{-3}, which correspond to the $p\text{-}n^+$ configuration. The carrier doping ratio (electron density in buffer/hole density in CFO absorber) of 100 is observed to be the optimal condition.

The efficiency of the CFO device increases with decreasing defect density, as shown in the simulated plot in Fig. 7a. At low absorber bulk defect density, the performance is better for higher absorber thickness. It is observed that lower absorber thickness performs better than high absorber thickness under high defect density, as shown in the inset plot of Fig. 7a. Efficiency exhibits an inverse relationship with defect density and a direct relationship with thickness. As a result, there is a trade-off between these two design parameters. A low thickness is preferred when dealing with high defect density, while a higher

Fig. 6 The simulated plot showing the efficiency as the function of majority carrier density in absorber and buffer layer in CuFeO$_2$/ZnO/ITO device
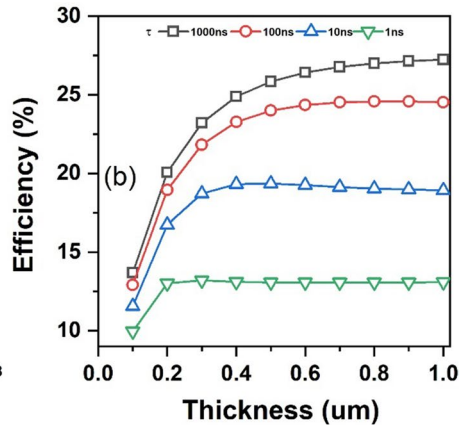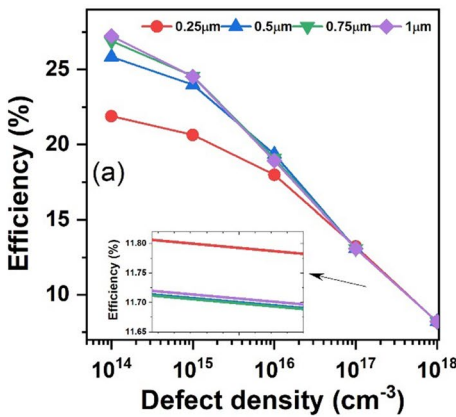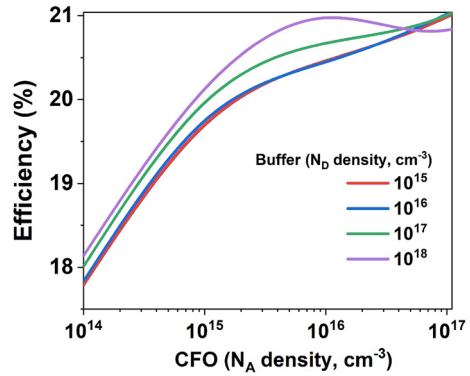

Fig. 7 a The efficiency of the CFO device as a function of bulk defect density for various absorber thicknesses. **b** The efficiency as a function of absorber thickness for various carrier lifetimes in CFO

thickness is the optimal design rule for a lower defect density in the device. The device performance is simulated under the impact of varied carrier lifetime and the thickness of the CFO absorber layer. Figure 7b shows the performance parameters, viz. efficiency, for τ variation from 1 to 1000 ns. The non-radiative Shockley–Read–Hall (SRH) recombination is directly proportional to the defect density (N_T) and inversely proportional to the carrier lifetime as given by Chowdhury et al. (2020)

$$R_{SRH} = \frac{v_{th}N_T\sigma_n\sigma_p\left[np - n_0p_0\right]}{\tau_n\left[p + p_1\right] + \tau_p\left[n + n_1\right]} \tag{9}$$

The v_{th} is electron thermal velocity, σ_n and σ_p capture cross-sections for electrons and holes, N_T defect density, n_i intrinsic density, n and p concentrations of electrons and holes at equilibrium, and n_1 and p_1 concentrations of electrons and holes in trap defects and valence band, respectively. When the defect density exceeds a certain threshold (beyond 10^{16} cm^{-3}), bulk recombination becomes dominant, leading to the annihilation of charge
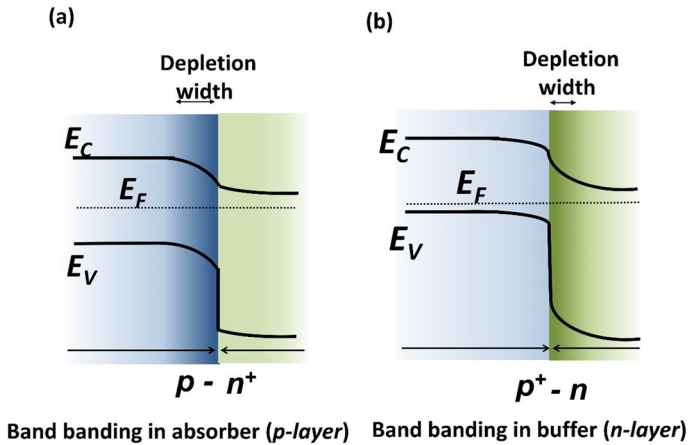
Fig. 8 **a** The cliff-type conduction band offset alignment shows elevated interfacial recombination through the absorber/buffer interface states. **b** The spike-type conduction band offset alignment shows a wider interfacial gap and reduced interfacial recombination

carriers. This significantly affects the efficiency, causing a sharp decline, as observed in Fig. 7. Reducing the absorber layer's thickness can effectively mitigate the impact of such high defect density. The reduced thickness of the absorber could minimize recombination but result in reduced J_{SC}. An optimized thickness is required for maximized performance by trade-off between J_{SC} and recombination.

The doping profile in the absorber and buffer layer controls the position of the Fermi energy levels, bend bending and drift field at the junction (Klenk 2001; Kumar and Thakur 1953). Different doping profiles (p–n^+ and p^+–n) and their comparative energy band diagram are shown in Fig. 8. It is observed that the majority of energy bending occurred in the doped layer. The corresponding doping profile of p–n^+ is a hole density of 10^{15} cm^{-3} in *the p*-layer and an electron density of 10^{18} cm^{-3} in the n^+-layer. Similarly, *the p^+–n* junction has a doping profile of hole density of 10^{18} cm^{-3} in *the p^+*–layer and electron density of 10^{15} cm^{-3} in n-layer. This asymmetric doping profile could manoeuvre the device's band bending profile and drift field and tune interfacial recombination. Energy band bending provides drift to photogenerated carriers and is advantageous for their collection. Under illumination, the photogenerated electrons in the p absorber of *the p–n^+* device go through this additional drift field and are efficiently collected in the buffer layer. This increases collection efficiency and reduces the interfacial recombination probability. This bending becomes crucial for charge extraction as it aids carrier diffusion length and active absorption region. The p^+n configuration causes band bending in n-region. This bending in the wide band gap buffer region significantly lowers the n-layer conduction band level, creating a probable recombination channel for the valence band hole in the p^+ layer and the conduction band electron in the n-layer.

3.3 Performance under various recombination regime

The device's extrinsic losses include the back contact, parasitic resistances, surface recombination velocity, and SRH non recombination (V_{OC}). Impact of various design parameter on CFO device performance is summarised in Table 3 (Kumar and Ranjan 2021; Pan et al.

Table 3 Impact of various design parameters on CFO device performance (Kumar and Ranjan 2021; Pan et al. 2006; Kumar and Thakur 2019; Wang et al. 2019)

	Impact of bulk defect density	Impact of back contact work function	Impact of resistance	Impact of Surface recombination velocity
Observed impact	V_{Loss} increases with high defect density. Efficiency decreases with increasing V_{Loss}	V_{OC} decreases and saturates for high back contact barrier; Efficiency decreases with low back contact work function	FF decreases for low shunt resistance. Efficiency decreases with suboptimal resistances	V_{OC} is lowered by a constant level for high SRV
Mathematical eq	$R_{SRH} = \frac{v_{th} N_T \sigma_n \sigma_p [np-n_o p_o]}{\tau_n[p+p_1]+\tau_p[n+n_1]}$ (53) $V_{Loss}=E_G/q\text{-}V_{OC}$	$V_{output}=V_{p\text{-}n}\text{-}V_{back}$ (57) $I_{Schockley}=I_L-I_0(e^{\frac{qV}{nkT}}-1)-\frac{V}{R_{SH}}$ $I_{Schottky}=I_0^* exp\left[-\frac{q\phi_B}{kT}\right]\left(exp\frac{qV}{akT}-1\right)$	$V = \frac{nKT}{q}\ln\frac{I_L-I-\frac{V}{R_{SH}}}{I_o}$ (56) $FF_{sh}=FF_o\left(1-\frac{v_{oc}+0.7}{v_{oc}}\frac{FF_o}{r_{sh}}\right)$	$\tau_S = \frac{W}{2S}+\frac{1}{D}\left(\frac{W}{\pi}\right)^2$ (59) $\frac{1}{\tau_{ff}}=\frac{1}{\tau_b}+\frac{1}{\tau_S}$
Physical explanation	The recombination mechanism depends on defect density ($R_{SRH} \propto N_T$), primarily trap-assisted recombination. At higher defect density, V_{OC} decreases, increasing the voltage loss (V_{Loss})	It is observed that the V_{OC} and efficiency decrease with lower work function of back contact. The low work function induces a Schottky barrier (non-ohmic back contact), which is aligned opposite to the p–n junction in the device. Voltage drop (V_{back}) across the back contact Schottky barrier is opposite to that induced by the p–n junction (V_{p-n})	Shunt resistance R_{SH} signifies the internal recombination in the device. It causes high internal recombination and FF degradation for low R_{SH}. Series resistance (R_S) offers electrical resistance, which limits J_{SC} and FF	V_{OC} is directly proportional to the effective lifetime. High SRV lowers the effective lifetime as given by eq. above. Thus, low SRV values are obtained by passivated contact and result in higher device performance

2006; Kumar and Thakur 2019). Figure 9 shows the efficiency waterfall of the CFO for various extrinsic losses. The CFO/ZnO/ITO configuration has near ohmic front contact due to high carrier concentration in the *n*-type window layer. The *p*-type semiconductor has a stringent requirement of high work function (greater than the electron affinity and bandgap of the absorber combined) for near ohmic contact. Thus, very few materials with high work function are suitable to obtain a near ohmic contact with a *p*-type semiconductor. The back contact work function dependence is summarised as the bar chart in Fig. 9. Simulation results show that device efficiency falls steeply with decreased back contact work function (BCWF). CFO/ZnO device showed efficiency > 28% for electron affinity above 5.5 eV of rear contact. Another parameter of contact quality is surface recombination velocity. Efficiency falls to 11% for electron affinity ~ 5.0 eV of rear contact. Another crucial metric of contact quality is surface recombination velocity (SRV). The efficiency dependence on SRV is summarized in Fig. 9 bar chart. Here, we quantify the range of surface recombination velocities that would allow the CFO solar cell to reach power conversion efficiencies above 25%. SRV less than 100 cm/s enable efficiency above 28%. It is observed that SRV as high as 10^4 cm/s is acceptable without much degradation on the CFO/ZnO solar cell. Passivated contacts in Si possess SRV below 10 cm/s, perovskite materials showed similar SRV values (Wang et al. 2019). The bar chart plot summarises the electrical loss due to parasitic resistance of series resistance (R_S) and shunt resistance (R_{SH}). Series resistance (R_S) offers electrical resistance, which limits J_{SC} and FF. Shunt resistance (R_{SH}) signifies the internal recombination in the device. It causes high internal recombination and FF degradation for low (R_{SH}). The performance ceiling of the device under trap-assisted non-radiative SRH recombination is simulated. The increased defect density in the absorber accelerates the SRH recombination such induced recombination causes V_{Loss}, where $V_{Loss} = E_G/q - V_{OC}$. The ideal device will have a V_{Loss} of 0.3 V. The general V_{Loss} in the experimental device is observed to be 0.5 V in perovskite, 0.6 V in CIGS, CdTe and 0.7 V in CZTS solar cell devices. We simulated a loss of 0.5 to 0.7 for the CFO device and observed the corresponding efficiency. With open circuit voltage loss V_{Loss} of 0.4, 0.5, 0.6 and 0.7 V, the simulated efficiency is 28%, 17.8%, 12% and 8.4%, respectively. Table 4 summarizes the V_{OC}, FF and J_{SC} for various V_{Loss} of 0.4–0.7 V. Apart from V_{OC}, FF is severely affected by increased V_{Loss}. The comparative V_{Loss} of 0.5 V and 0.6 V for increased bulk defect density in the absorber have highlighted the importance of controlling defects. Restricting resistance and SRH losses is crucial for achieving high performance in CFO device.

3.4 Optimized performance of CuFeO₂ solar cell

The theoretical maximum efficiency corresponding to the absorber with a bandgap of 1.5 eV is 31.7%. CFO final device with a description of incident energy utilization in the conversion process as shown in Fig. 10. The spectrum loss, which consists of thermalization and transmission losses, stands at 59.6% for CFO/ZnO/ITO device with absorber bandgap of 1.5 eV. The extrinsic recombination due to electrical loss of parasitic resistance R_S and R_{Sh}, non-ideal mobility, SRV, non-ohmic contact, etc., stands at 3.6% in this optimized configuration. The intrinsic radiative recombination is observed to be 8.7%, comprised of intrinsic loss such as radiation dilution, entropy generation, etc. The net useful efficiency, which is the remainder of incident solar energy from all the losses, stands at 28.1%. After selecting a suitable buffer counterpart, the CFO device, absorber thickness, defect density optimization, contact, and SRV optimization showed 28.1% performance.
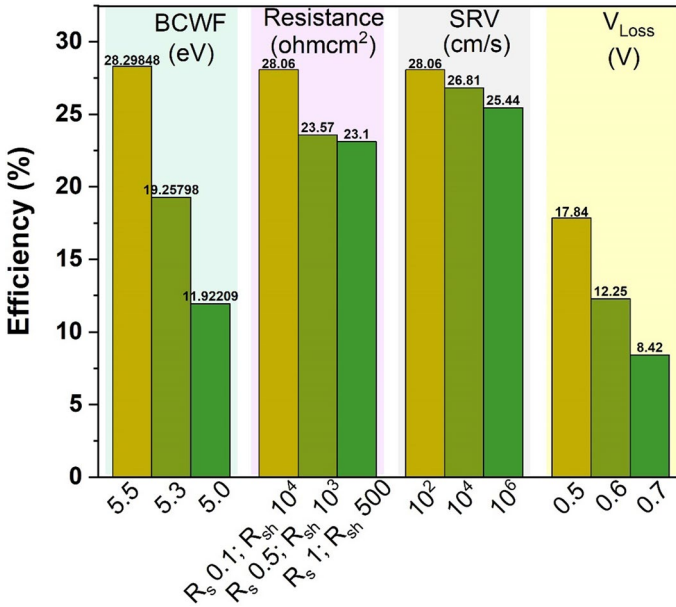
Fig. 9 Efficiency bar chart for various extrinsic efficiency limiting factors such as contact work function, parasitic resistance, surface recombination velocity and V_{Loss}

Table 4 Summary of the computed performance parameter of CFO device for various V_{Loss}

	Efficiency (%)	FF (%)	J_{SC} (mA/cm^2)	V_{OC} (V)
SQ limit values (Eg = 1.5 eV)	31.64	89.90	28.97	1.21
V_{Loss} = 0.4	25	86	26.5	1.1
V_{Loss} = 0.5	17.84	75.59	23.56492	1.0018
V_{Loss} = 0.6	12.25	67.97	19.99044	0.9012
V_{Loss} = 0.7	8.42	62.67	16.72072	0.8037

Theoretical analysis shows that optimized device configuration can significantly reduce recombination, resulting in improved performance.

The final current density vs voltage J-V plot is shown in Fig. 11a. The final performance parameter of the CFO/ZnO/ITO device stand at $V_{OC} = 1.14$ eV, $J_{SC} = 27$ mA/cm^2, FF = 88% and efficiency = 28.06%. The external quantum efficiency EQE is shown in Fig. 11b. The EQE is optimal in the 400–800 nm wavelength range and shows an absorption onset near 825 nm wavelength. Higher wavelengths than this are transmitted and non-absorbed. Wavelength regions from 825 to 400 nm are showing near 100% EQE. The external quantum efficiency refers to how the photovoltaic device reacts to different wavelengths of light, which can be used to determine the net short circuit current density J_{SC}. The net short circuit current could be estimated from the product of quantum efficiency (QE) and the solar spectrum. In the 300–400 nm wavelength range, a decrease in quantum efficiency is

Fig. 10 The pie chart shows the portion of incident solar energy lost as spectrum loss (thermalization and non-absorption loss), intrinsic loss, extrinsic recombination loss and the remaining portion available for useful efficiency of the optimized device
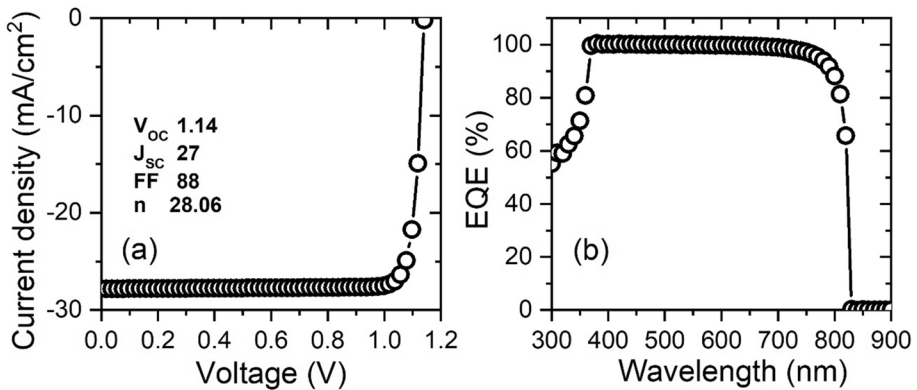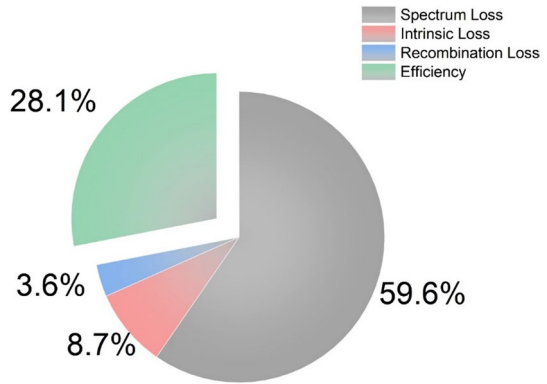

Fig. 11 a The simulated JV plot of the optimized CFO device. **b** The final optimized EQE plot

noticed because of unwanted absorption occurring in the electron transport layer (ETL) and hole transport layer (HTL).

The detailed balance efficiency limit, or the Schockley-Queisser (SQ) limit, represents the theoretical maximum efficiency achievable and depends on the band gap. The SQ limit of efficiency and 60% of efficiency as a function of the bandgap is plotted in Fig. 12. The experimentally reported efficiency of the contemporary solar cells is compared with the SQ limit values. The predicted efficiency of CFO is 28%, comparable to the leading inorganic photovoltaic technologies of Si, GaAs, and CsPbI$_3$ perovskites. CFO is an inorganic, nontoxic, earth-abundant and stable absorber with promising prospects as solar cells. Theoretical analysis showed that CFO/ZnO/ITO device is achieving 88.5% of the theoretical value (SQ limit) for an absorber corresponding to the bandgap of 1.5 eV.

4 Conclusion

The earth-abundant, nontoxic delafossite CuFeO$_2$ absorber-based solar cell is optimized by SCAPS 1D. We first explored an efficient buffer counterpart from a host of available *n*-type materials to form an efficient heterojunction with CFO. Wide bandgap ZnO is found to be
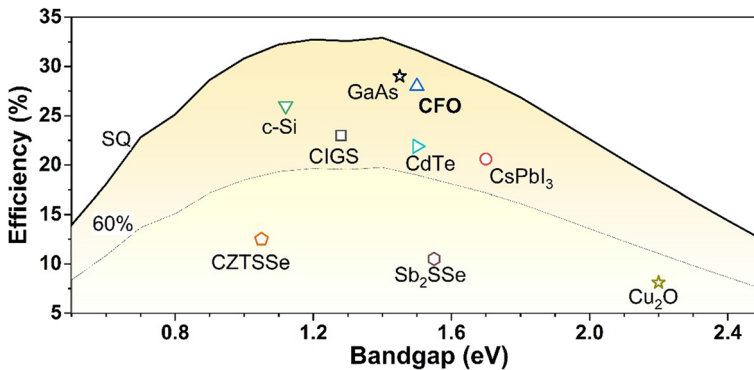
Fig. 12 The SQ limit comparison of the contemporary inorganic solar cells with the proposed earth-abundant, inorganic, cost-effective CFO absorber. (Zakutayev et al. 2021; Green et al. 2023; Almora et al. 2021)

a compatible heterojunction counterpart based on its suitable bandgap, electron affinity and high electron carrier density. We assessed this CFO-based device under different recombination regimes to identify efficiency limiting factors, theoretical maximum efficiency, and optimal device design. The stack of $CuFeO_2$/ZnO/ITO with p-n^+-n^{++} configuration is optimal and showed an efficiency of 28%. The findings presented in this study are anticipated to inspire researchers to create stable, high-efficiency CFO-based thin film solar cells.

Declarations

References

Akin, S., Sadegh, F., Turan, S., Sonmezoglu, S.: Inorganic CuFeO2 delafossite nanoparticles as effective hole transport material for highly efficient and long-term stable perovskite solar cells. ACS Appl. Mater. Interfaces **11**(48), 45142–45149 (2019)

Alkallas, F.H., Ben Gouider Trabelsi, A., Alrebdi, T.A., Ahmed, A.M., Rabia, M.: Development of a highly efficient optoelectronic device based on $CuFeO_2$/CuO/Cu composite nanomaterials. Materials **15**, 6857 (2022)

Almora, O., Baran, D., Bazan, G.C., Berger, C., Cabrera, C.I., Catchpole, K.R., Erten-Ela, S., Guo, F., Hauch, J., Ho-Baillie, A.W.Y., Jesper-Jacobsson, T., Janssen, R.A.J., Kirchartz, T., Kopidakis, N., Li, Y., Loi, M.A., Lunt, R.R., Mathew, X., McGehee, M.D., Min, J., Mitzi, D.B., Nazeeruddin, M.K., Nelson, J., Nogueira, A.F., Paetzold, U.W., Park, N.G., Rand, B.P., Rau, U., Snaith, H.J., Unger, E.,

Vaillant-Roca, L., Yip, H.L., Brabec, C.J.: device performance of emerging photovoltaic materials (Version 2). Adv. Energy Mater. **11**, 2102526 (2021)

Burgelman, M., Nollet, P., Degrave, S.: Modelling polycrystalline semiconductor solar cells. Thin Solid Films **361–362**, 527–532 (2000)

Chowdhury, M.S., Shahahmadi, S.A., Chelvanathan, P., Tiong, S.K., Amin, N., Techato, K., Nuthammachot, N., Chowdhury, T., Suklueng, M.: Effect of deep-level defect density of the absorber layer and n/i interface in perovskite solar cells by SCAPS-1D. Results Phys. **16**, 102839 (2020)

Crespo, C.T.: Potentiality of $CuFeO_2$-delafossite as a solar energy converter. Sol. Energy **163**, 162–166 (2018)

Dandogbessi, B.S., Akin-Ojo, O.: First-principles prediction of the electronic structure and carrier mobilities of biaxially strained molybdenum trioxide (MoO_3). J. Appl. Phys. **120**(5), 055105 (2016)

Deng, Q., Shi, L., Lu, K., Wang, G., Di, T., Shen, Y., Wang, S.: Construction of Ca-$CuFeO_2$/TiO_2(B) p–n heterojunctions with efficient visible light-driven photocatalysis. The Journal of Physical Chemistry C **127**(9), 4704–4713 (2023). https://doi.org/10.1021/acs.jpcc.2c08064

Egbo, K.O., Shil, S.K., Kwok, C.G., Wang, Y., Liu, C.P., Yu, K.M.: Band alignment of wide bandgap NiO/MoO3 and NiO/WO3 p-n heterojunctions studied by high-resolution X-ray photoelectron spectroscopy. J. Alloy. Compd. **876**, 160136 (2021)

Elumalai, N.K., Vijila, C., Jose, R., et al.: Metal oxide semiconducting interfacial layers for photovoltaic and photocatalytic applications. Mater. Renew. Sustain. Energy **4**, 11 (2015). https://doi.org/10.1007/s40243-015-0054-9

Ferri, M., Elliott, J., Fabris, S., Piccinin, S.: Establishing best practices to model the electronic structure of $CuFeO_2$ from first principles. Phys. Rev. B **101**, 155201 (2020)

Forslund, A.: Synthesis and characterization of delafossite $CuFeO_2$ for solar energy applications, PhD thesis, Uppsala Universitet (2016)

Fugate, E.A., Biswas, S., Clement, M.C., Kim, M., Kim, D., Asthagiri, A., Baker, L.R.: The role of phase impurities and lattice defects on the electron dynamics and photochemistry of $CuFeO_2$ solar photocathodes. Nano Res. **12**, 2390–2399 (2019)

Gomathi, S., Sivapriya, J., Kalaiyarasi, M., Sivakumar, J., Jaanaa Rubavathy, S., Kumar, A.: Analyzing the performance ceiling of $RbSnGeI_3$ -based lead-free stable perovskite solar cell. Opt. Quant. Electron. **55**, 734 (2023a)

Gomathi, S., Raj, A.G., Mishra, C.S., Kumar, A.: Straddling type sandwiched absorber based solar cell structure. Optik **272**, 170354 (2023b)

Gonzaga, I.L.E., Mercado, C.C.: Copper ternary oxides as photocathodes for solar-driven CO_2 reduction. Rev. Adv. Mater. Sci. **61**(1), 430–457 (2022)

Gottesman, R., Levine, I., Schleuning, M., Irani, R., Abou-Ras, D., Dittrich, T., Friedrich, D., van de Krol, R.: Overcoming phase-purity challenges in complex metal oxide photoelectrodes: a case study of CuBi2O4. Adv. Energy Mater. **11**, 2003474 (2021)

Green, M.A., Dunlop, E.D., Yoshita, M., Kopidakis, N., Bothe, K., Siefer, G., Hao, X.: Solar cell efficiency tables (version 62). Prog. Photovolt. Res. Appl. **31**(7), 651–663 (2023)

Hemalatha, S., Prabu, R.T., Radhika, R., Kumar, A.: Dual-absorber thin-film solar cell: a high-efficiency design. Phys. Status Solidi A **220**, 2200761 (2023)

Jiang, C.M., Reyes-Lillo, S.E., Liang, Y., Liu, Y.S., Liu, G., Toma, F.M., Prendergast, D., Sharp, I.D., Cooper, J.K.: Electronic Structure and Performance Bottlenecks of $CuFeO_2$ Photocathodes. Chem. Mater. **31**(7), 2524–2534 (2019a)

Jiang, T., Zhao, Y., Xue, H.: Boosting the performance of delafossite photocathode through constructing a CuFeO2/CuO heterojunction for photoelectrochemical water reduction. J. Mater. Sci. **54**, 11951–11958 (2019b)

Jin, Y., Chumanov, G.: Solution synthesis of pure 2H $CuFeO_2$ at low temperatures. RSC Adv. **6**, 26392–26397 (2016)

Kang, M., Jung, J., Lee, S.Y., Ryu, J.W., Kim, S.W.: Conductivity, carrier density, mobility, seebeck coefficient, and power factor in V2O5. Thermochim. Acta **576**, 71–74 (2014)

Kar, M., Sarkar, R., Pal, S., Sarkar, P.: Lead-free two-dimensional mixed tin and germanium halide perovskites for photovoltaic applications. J. Phys. Chem. C **125**, 74–81 (2021)

Karmakar, K., Sarkar, A., Mandal, K., Khan, G.G.: Nano-engineering of *p-n* $CuFeO_2$-ZnO heterojunction photoanode with improved light absorption and charge collection for photoelectrochemical water oxidation. Nanotechnology **28**, 325401 (2017)

Klenk, R.: Characterisation and modelling of chalcopyrite solar cells. Thin Solid Films **387**, 135–140 (2001)

Kumar, A., Ajay, D.: Thakur Role of contact work function, back surface field, and conduction band offset in Cu_2ZnSnS_4 solar cell. Jpn. J. Appl. Phys. **57**, 08RC05 (2018)

Kumar, A., Ranjan, P.: Defects signature in V_{OC} characterization of thin-film solar cells. Sol. Energy **220**, 35–42 (2021)

Kumar, A., Thakur, A.D.: Design issues for optimum solar cell configuration. AIP Conf. Proc. **1**, 050022 (1953)

Kumar, A., Thakur, A.D.: Comprehensive loss modeling in Cu_2ZnSnS_4 solar cells. Curr. Appl. Phys. **19**, 1111–1119 (2019)

Kumar, A., Singh, N.P., Sundaramoorthy, A.: Comparative device performance of CZTS solar cell with alternative back contact. Mater. Lett. X **12**, 100092 (2021)

Kumar, A., Prabu, R.T., Das, A.: Configuration analysis of SnS-based solar cells for high-efficiency devices. Opt. Quant. Electron. **54**, 521 (2022)

Lee, D., Park, J.W., Cho, N.K., et al.: Verification of charge transfer in metal-insulator-oxide semiconductor diodes via defect engineering of insulator. Sci. Rep. **9**, 10323 (2019)

Li, R.P., Shan, B.F., Zhao, Z.Y.: Delafossite $CuFeO_2$ nanosheets with highly exposed 001 crystal facets for enhancing charge separation efficiency. Appl. Surf. Sci. **618**, 156594 (2023)

Liu, X., Zheng, H., Zhang, J., Xiao, Y., Wang, Z.: Photoelectric properties and charge dynamics for a set of solid-state solar cells with $Cu_4Bi_4S_9$ as the absorber layer. J. Mater. Chem. a. **1**, 10703–10712 (2013)

Liu, Q.L., Zhao, Z.Y., Zhao, R.D., Yi, J.H.: Fundamental properties of delafossite $CuFeO_2$ as photocatalyst for solar energy conversion. J. Alloy. Compd. **819**, 153032 (2020a)

Liu, Q.L., Zhao, Z.Y., Yi, J.H.: Excess oxygen in delafossite $CuFeO_2+\delta$: Synthesis, characterization, and applications in solar energy conversion. Chem. Eng. J. **396**, 125290 (2020b)

Livingston, L.M.M., Raj, A.G.S., Prabu, R.T., et al.: Computational analysis of FeS_2 material for solar cell application. Opt. Quant. Electron. **55**, 244 (2023)

Medhi, R., Li, C.H., Lee, S.H., Marquez, M.D., Jacobson, A.J., Lee, T.C., Lee, T.R.: Uniformly spherical and monodisperse antimony- and zinc-doped tin oxide nanoparticles for optical and electronic applications. ACS Appl. Nano Mater. **2**(10), 6554–6564 (2019)

Minemoto, T., Murata, M.: Theoretical analysis on effect of band offsets in perovskite solar cells. Sol. Energy Mater. Sol. Cells **133**, 8–14 (2015)

Pan, J., Gloeckler, M., Sites, J.R.: Hole current impedance and electron current enhancement by back-contact barriers in CdTe thin film solar cells. J. Appl. Phys. **100**, 124505 (2006)

Prabu, R.T., Malathi, S.R., Kumar, A., Al-Asbahi, B.A., Laref, A.: Bandgap assessment of compositional variation for uncovering high-efficiency improved stable all-inorganic lead-free perovskite solar cells. Phys. Status Solidi A **220**, 2200791 (2023)

Prévot, M.S., Guijarro, N., Sivula, K.: Enhancing the performance of a robust sol–gel-processed p-type delafossite $CuFeO_2$ photocathode for solar water reduction. Chemsuschem **8**, 1359–1367 (2015)

Prévot, M.S., Jeanbourquin, X.A., Bourée, W.S., Abdi, F., Friedrich, D., van de Krol, R., Guijarro, N., Le Formal, F., Sivula, K.: Evaluating charge carrier transport and surface states in $CuFeO_2$ photocathodes. Chem. Mater. **29**(11), 4952–4962 (2017)

Reddy, Y.K., Manjunath, V., Bimli, S., Devan, R.S.: Futuristic kusachiite solar cells of $CuBi_2O_4$ absorber and metal sulfide buffer Layers: theoretical efficiency approaching 28 %. Sol. Energy **244**, 75–83 (2022)

Ryu, J.H., You, Y.G., Kim, S.W., Hong, J.H., Na, J.H., Jhang, S.H.: Effect of Al_2O_3 deposition on carrier mobility and ambient stability of few-layer MoS2 field effect transistors. Curr. Appl. Phys. **20**(2), 363–365 (2020)

Scanlon, D., Dunnill, C., Buckeridge, J., et al.: Band alignment of rutile and anatase TiO_2. Nat. Mater. **12**, 798–801 (2013)

Shaili, H., Salmani, E., Beraich, M., Elhat, A., Rouchdi, M., Taibi, M., Ez-Zahraouy, H., Hassanain, N., Mzerd, A.: Revealing the impact of strontium doping on the optical, electronic and electrical properties of nanostructured 2H-$CuFeO_2$ delafossite thin films. RSC Adv. **11**, 25686 (2021)

Shi, J., Zhang, J., Yang, L., Qu, M., Qi, D.C., Zhang, K.H.: Wide bandgap oxide semiconductors: from materials physics to optoelectronic devices. Adv. Mater. **33**, 2006230 (2021). https://doi.org/10.1002/adma.202006230

Singh, G., Kaur, T.P., Tangra, A.K.: Novel $KFeO_2$ nanoparticles for dye-sensitized solar cell. Mater. Res. Express **6**, 1150f5 (2019)

Singh, A.P., Wang, R.B., Tossi, C., Tittonen, I., Wickman, B., Hellman, A.: Hydrogen induced interface engineering in Fe_2O_3–TiO_2 heterostructures for efficient charge separation for solar-driven water oxidation in photoelectrochemical cells. RSC Adv. **11**, 4297–4307 (2021)

Son, M.-K.: Effect of deposition parameters on morphological and compositional characteristics of electrodeposited $CuFeO_2$ film. Coatings **12**(12), 1820 (2022a). https://doi.org/10.3390/coatings12121820

Son, M.-K.: Effect of deposition parameters on morphological and compositional characteristics of electrodeposited $CuFeO_2$ Film. Coatings **12**, 1820 (2022b). https://doi.org/10.3390/coatings12121820

Song, J.D., Wu, J.C., Rao, X., Li, S.J., Zhao, Z.Y., Liu, X.G., Zhao, X., Sun, X.F.: Single crystal growth of $CuFe_{1-x}Ga_xO_2$ by the optical floating-zone method. J. Cryst. Growth **446**, 79–84 (2016)

Stangl, R., Kriegel, M., Schmidt, M.: AFORS-HET, Version 2.2, a numerical computer program for simulation of heterojunction solar cells and measurements. In: Proc. WCPEC-4, 4th world conference on photovoltaic energy conversion, Hawaii, May (2006). https://doi.org/10.1109/WCPEC.2006.279681

Vojkovic, S., Fernandez, J., Elgueta, S., Vega, F.E., Rojas, S.D., Wheatley, R.A., Seifert, B., Wallentowitz, S., Cabrera, A.L.: Band gap determination in multi-band-gap $CuFeO_2$ delafossite epitaxial thin film by photoconductivity. SN Appl. Sci. **1**, 1322 (2019)

Wang, J., Fu, W., Jariwala, S., Sinha, I., Jen, A.K., Ginger, D.S.: Reducing surface recombination velocities at the electrical contacts will improve perovskite photovoltaics. ACS Energy Lett. **4**(1), 222–227 (2019)

Xu, H., Wu, R., Zhang, J.Y., Han, W., Chen, L., Liang, X., Haw, C.Y., Mazzolini, P., Bierwagen, O., Qi, D.C., Zhang, K.H.: Revealing the electronic structure and optical properties of $CuFeO_2$ as a p-type oxide semiconductor. ACS Appl. Electron. Mater. **3**(4), 1834–1841 (2021)

Zakutayev, A., Major, J.D., Hao, X., Walsh, A., Tang, J., Todorov, T.K., Wong, L.H., Saucedo, E.: Emerging inorganic solar cell efficiency tables (version 2). J. Phys. Energy. **3**, 032003 (2021)

Zhu, T., Deng, Z., Fang, X., Huo, Z., Wang, S., Dong, W., Shao, J., Tao, R., Song, C., Wang, L.: High photovoltages of CuFeO2 based p-type dye-sensitized solar cells. J. Alloys Comp. **685**, 836–840 (2016)

Authors and Affiliations

D. Prasad[1] · G. Anitha[2] · L. Megalan Leo[3] · Atul Kumar[4]

✉ Atul Kumar
er.atul89@gmail.com

D. Prasad
mani.gd@gmail.com

G. Anitha
anipsg09@gmail.com

L. Megalan Leo
megalanleo@gmail.com

[1] Department of Electrical and Electronics Engineering, Sona College of Technology, Salem 636005, India

[2] Department of Electronics and Communication Engineering, Saveetha School of Engineering, Saveetha Institute of Medical and Technical Sciences, Chennai 602105, India

[3] Department of Electronics and Communication Engineering, Sathyabama Institute of Science and Technology, Chennai 600119, India

[4] Department of Electronics and Communication Engineering, Koneru Lakshmaiah Education Foundation, Greenfields, Vaddeswaram, Guntur, Andhra Pradesh 522502, India